OPTICAL QUALITY CHARACTERIZATION OF KDP CRYSTALS WITH INCORPORATED TiO_2 NANOPARTICLES AND LASER SCATTERING EXPERIMENT SIMULATION

V.YA. GAYVORONSKY,[1] V.N. STARKOV,[1] M.A. KOPYLOVSKY,[1] M.S. BRODYN,[1] E.A. VISHNYAKOV,[1] A.YU. BOYARCHUK,[1] I.M. PRITULA[2]

[1]Institute of Physics, Nat. Acad. of Sci. of Ukraine
(46, Nauky Prosp., Kyiv 03680, Ukraine; e-mail: vlad@iop.kiev.ua)

[2]STC "Institute for Single Crystals", Nat. Acad. of Sci. of Ukraine
(60, Lenin Ave., Kharkiv 61001, Ukraine)

PACS 78.20.-e, 42.25.Fx, 02.30.Cj, 78.67.Bf, 42.70.Mp

We study the elastic scattering of light in pure KDP crystals and KDP crystals with incorporated titanium dioxide nanoparticles. It is shown that the optical quality of the crystals decreases insufficiently for the used concentrations of nanoparticles. A mathematical model of the experimental setup for light scattering measurements in low-dispersion media is developed and discussed. The propagation function of the experimental setup is given in analytical form. The relevance of the model is verified with the use of experimental scattering data.

1. Introduction

The paper is devoted to the optical quality characterization of the novel nonlinear optical (NLO) material – potassium dihydrogen phosphate single crystal (KH_2PO_4, KDP) matrix with incorporated titanium dioxide nanocrystals (anatase modification) [1]. The hybrid material was designed for the phase matching conditions and the second harmonic generation efficiency control by light due to the resonant excitation of the surface states of nanoparticles [2]. We applied the cone-shaped interference method to study the effect of TiO_2 nanoparticles on the linear optical response of the medium. A special attention was paid to investigate the angular distribution of scattered light (scattering indicatrix) and scattering extinction losses for a highly transparent low-dispersion NLO functional material.

Experimental data on scattering in low-dispersion materials are within a high dynamic range (6–7 orders of the signal magnitude). To enable the measurements of weak signals of the scattered light, we use a collecting lens on the registration CCD array with the angular aperture that essentially exceeds the initial divergence of a laser beam. This leads to an enhancement of the signal-to-noise ratio at large scattering angles and simultaneously to the angular averaging of registered data. The introduction of the experimental setup apparatus function gives possibility to derive the precise angular signal distribution using a proper mathematical processing of experimental data.

Previously, a mathematical model was developed in [3]. It was shown that the registered scattering signal is distorted at small scattering angles. That model can be applied to high-dispersive media like that described in [4], but it is insufficient for low-dispersion samples due to the lacking of precision. For this reason, a more precise model of the experimental setup was developed. The consistency of the proposed model is verified, by using experimental measurements in series of the single crystal KDP matrix with different concentrations of TiO_2 nanocrystals [1].

2. Experimental Setup

For isotropic media, the scattering is axially symmetric, so it is sufficient to measure a cross-section of the light power/intensity angular distribution in any scattering plane (Fig. 1).

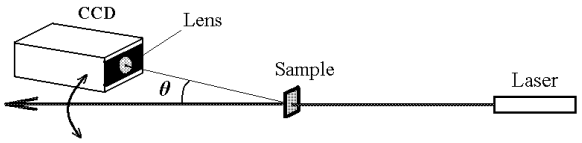

Fig. 1. Scheme of the experimental setup for angular dependence measurements of the scattered light. The lens mounted at a CCD array controls the solid angle for the scattering radiation collection, θ denotes the angle between the incidence laser beam and scattering signal acquisition directions

The experimental laser setup for the optical diagnostics of low-dispersion samples is based on a G-5 goniometer with different laser sources on its fixed arm: a DPSS diode laser (wavelength $\lambda = 532$ nm, radiation power $P = 50$ mW) or a He-Ne laser ($\lambda = 633$ nm, $P = 10$ mW). The sample under study is placed at a sample stage, and the registration unit is mounted on the movable arm of a goniometer at the distance $L = 200$ mm from the sample. It consists of a CCD array AMKO LTI MuLTIray (1024 pixels with 25×200 μm^2 pixel size, 12-bit digital resolution) with a lens (diameter $d = 9.6$ mm) attached to it. The rest receiving area of the CCD is completely blackened, so that only the light passed through the lens reaches the sensitive surface of the CCD array.

The experimental setup is intended for the investigation of a polar angular dependence of the scattered light power against to the incidence laser beam propagation direction. The magnitudes of radiation power along the registration direction θ in the given solid angle were obtained via the summation of the all pixels data of the CCD array. Due to the focusing lens, the signal on CCD is registered on a small number of pixels (~ 30) in each measurement, which extremely increases the signal-to-noise ratio.

The indicatrix registered with the use of this experimental setup is different from the real one due to the spatial averaging with the lens aperture. So it is reasonable to develop a mathematical route to restore the original angular distribution from the registered one. The model presented here is verified in a direct way, and it can be a base for solving the inverse problem in future.

Scattering data with high angular resolution are required for the verification of the model. This was achieved due to a reduction of the solid angle for the radiation collection. The CCD array with a wide aperture lens was replaced with a fiber coupled CCD spectrometer with the input fiber aperture ($d = 410$ μm). Unfortunately, the angular resolution enhancement leads to a drastic reduction of the scattering signal level and the angular range of data acquisition ($\theta \sim \pm 2^\circ$).

The spectroscopic and scattering measurements were done with crystalline plates $10 \times 10 \times 0.8$ mm^3 cut perpendicular to the optical axis (Z-cut) of the uniaxial KDP matrix. A set for the investigation consists of a pure KDP single crystalline plate and KDP crystals with incorporated TiO_2 nanoparticles at different concentrations (10^{-5}, 10^{-4}, and 10^{-3} wt.% TiO_2) in a mother liquor solution. There were two series KDP(Pr) and KDP(P) cut from the prismatic {100} and pyramidal {101} growth sectors, respectively. The pure KDP crystals will be denominated simply as P or Pr, and the rest of samples will be further designated according to the nomenclature in Table 1, where we also give the thickness h of each sample. In some cases, the TiO_2 nanoparticles concentration is written explicitly in a short form (e.g., 10^{-3} wt.%), which is referred to the nanoparticles concentration in the mother liquor solution.

Due to the opposite charge signs of the termination interfaces of the different growth sectors, the {101} (P) growth sector captures more TiO_2 nanocrystals in comparison with the {100} (Pr) sector at the growth stage. The preliminary research has shown that the average concentration of incorporated nanocrystals into the KDP matrix is twice less in comparison with the nanoparticles concentration in the mother liquor solution.

3. Mathematical Model, Experimental Results and Discussion

3.1. Optical quality characterization of crystals

3.1.1. Spectral transmittances

Optical transmittance spectra of the samples were measured with a Perkin Elmer Lambda 35 spectrometer in the range 200–1100 nm (the reference is air). The spec-

T a b l e 1. Spectral properties of the samples (measured with a fiber coupled spectrophotometer). "Pr" denotes the prismatic {100} growth sector, "P" — pyramidal {101}. TiO_2 concentrations are given for mother liquor solutions. h is the crystalline plate thickness

TiO_2 conc., wt.%	Sample notation	h, mm	Transmittance, %	
			$\lambda = 532$ nm	$\lambda = 633$ nm
0	P	0.81	91.3 ± 1.0	91.9 ± 0.9
	Pr	0.83	92.4 ± 0.6	93.0 ± 0.7
10^{-5}	P-5	0.75	89.8 ± 0.9	90.2 ± 1.1
	Pr-5	0.78	90.3 ± 0.9	91.0 ± 1.0
10^{-4}	P-4	0.76	89.8 ± 1.2	90.8 ± 1.0
	Pr-4	0.75	91.4 ± 1.1	92.0 ± 1.0
10^{-3}	Pr-3	0.81	89.1 ± 0.5	89.7 ± 0.5

tra were studied for the samples with polished (001) faces ∼0.8 mm in thickness without anireflective coatings.

The results of these spectral measurements are presented in Fig. 2, and the samples notations are given in Table 1. The transmittance magnitudes in the visible and near-IR ranges are governed, in principle, by the reflections from crystalline-air interfaces.

It is known that that the pure KDP crystals have different transmittances for prismatic (Pr) and pyramidal (P) growth sectors in the UV spectral range [1]. The P samples are more transparent due to a less efficient absorption of impurities from the mother liquor. In Fig. 2, we show a typical transmittance reduction ∼ 75 % at $\lambda = 270$ nm (curve *1*). Pr-5 and Pr-3 (curves *2* and *4*) have transmittances similar to that of the pure one in the range 260–350 nm, while Pr-4 (curve *3*) demonstrates a much higher transmittance in comparison with those of the rest ones. It gains ∼ 88% at 300 nm. The magnitude is comparable with the transmittance of the pure P crystal, and it exceeds the transmission of the pure Pr one by about 8%.

We suggest that the mentioned peculiarity can be explained due to the compensation effect of incorporated nanoparticles. For the prismatic growth sector, a concentration of 10^{-4} wt.% TiO_2 is not so high for the efficient absorption of UV light by anatase nanoparticles due to the direct transitions from the valence band to the conduction one. However, the concentration of incorporated nanoparticles is enough to absorb impurity atoms, especially the atoms of polyvalent metals on their developed surface during the growth stage.

We have also tested a homogeneity of the optical transmittances of crystals over the transverse plane with an Ocean Optics type fiber coupled spectrophotometer in the range 450–900 nm. The samples were illuminated with a broadband collimated light beam, and the readout of transmittances was performed with a microobjective attached to the fiber. It was placed at a distance of 2 mm from the crystal output interface, so it was possible to collect almost all the transmitted photons (both ballistic and diffusive ones). We performed 6–10 measurements for each sample. Their averaged transmission coefficients at 532 and 633 nm are presented in Table 1.

We selected the wavelengths for the characterization of optical homogeneity and scattering properties by the following reasons. The available laser sources at the mentioned wavelengths correspond to different regimes of the excitation of pure and hybrid materials. The wavelength $\lambda = 633$ nm corresponds to the nonresonant excitation of the KDP matrix and TiO_2 nanoparticles. The wavelength $\lambda =$ 532 nm leads to the resonance-type excitation for intrinsic matrix defects [5] and to the electron excitation from the valence band into the deep level of a defect in the gap (oxygen vacancies) of anatase nanoparticles [2].

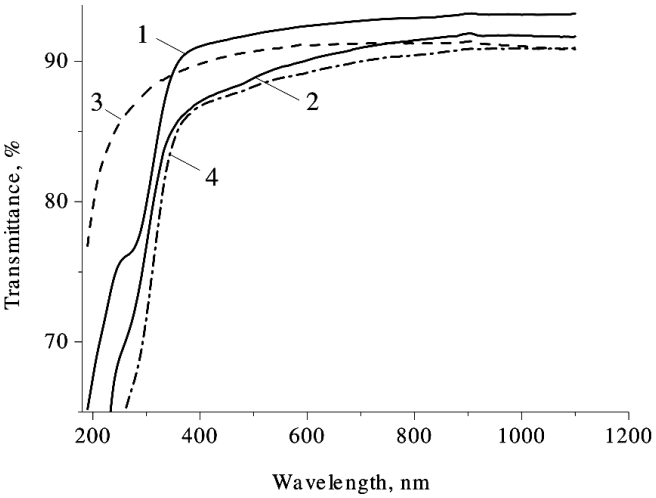

Fig. 2. Spectral transmittances of KDP single crystals with incorporated TiO_2 nanoparticles cut from the prismatic growth sector (Pr): *1* – pure KDP (Pr), *2* – KDP:TiO_2 with 10^{-5} wt.% (Pr-5), *3* – 10^{-4} wt.% (Pr-4), *4* – 10^{-3} wt.% (Pr-3) samples

The analysis of the data presented in Table 1 has shown that the nonresonant transmittance is a little bit higher than that in the resonance excitation case. A dispersion of the optical inhomogeneity is the most evident for the resonant excitation regime ($\lambda = 532$ nm) and for the 10^{-4} wt.% TiO_2 concentration. This can be explained by a high sensitivity of the compensation effect to the local concentration of anatase nanoparticles in the matrix.

The comparison of the data in Table 1 with the transmittance curves in Fig. 1 obtained with two different spectroscopic setups shows the high optical transmittance and the homogeneity of pure KDP and novel hybrid KDP:TiO_2 single crystals in the visible and near-IR ranges. We observed the ∼ 1% difference of the transmission coefficient for the investigated samples in the visible range. In the conventional mode of a Perkin Elmer spectrometer (without integrated sphere detection), the samples were placed at a distance of 200 mm from the 1×10 mm^2 slit of a detector unit. We explain the obtained minor magnitudes of the Perkin Elmer spectroscopic data by the presence of scattering losses, which was proved in the experiment dealing with scattering properties of the novel hybrid material.

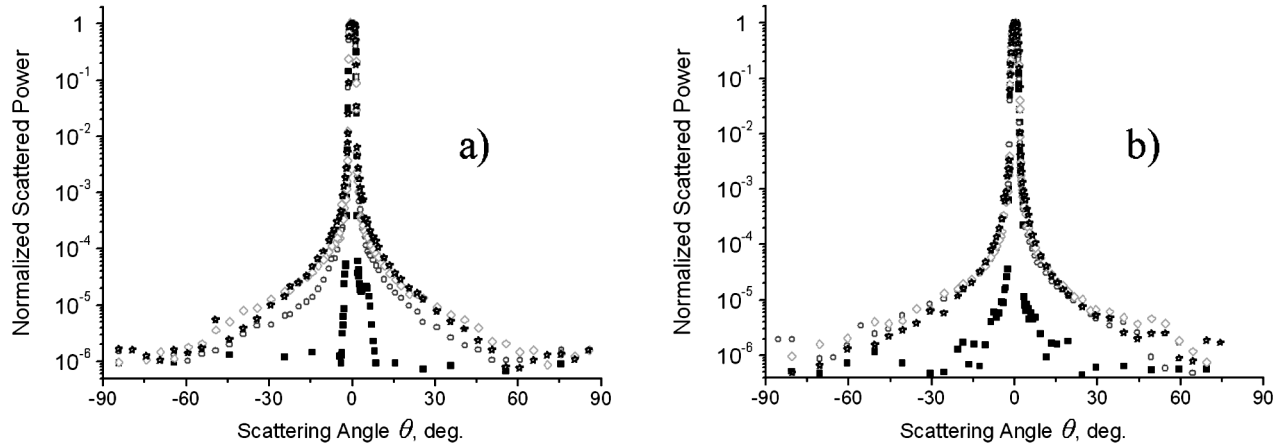

Fig. 3. Scattering indicatrices on the semilogarithmic scale for KDP(P) crystals series at (*a*) 532-nm and (*b*) 633-nm wavelengths. Squares – freely propagating laser beam; ○ – pure P crystal; ◇ – KDP:TiO_2 P-5 sample; ⋆ – KDP:TiO_2 P-4 sample

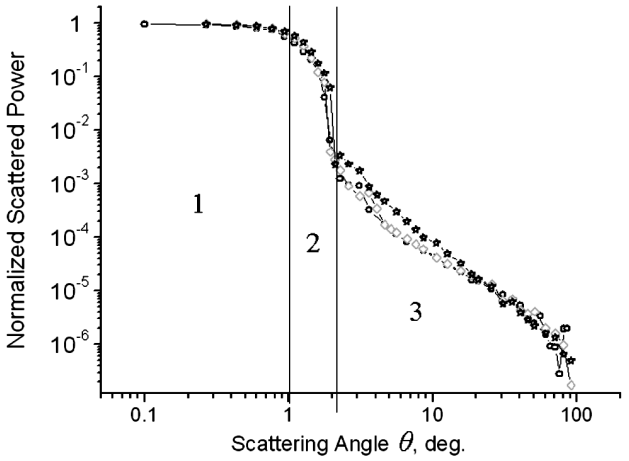

Fig. 4. Scattering indicatrices for the series of KDP(P) single crystals on the double logarithmic scale at 633 nm. ○ – pure P crystal, ◇ – KDP:TiO_2 P-5 sample, ⋆ – P-4 sample

3.1.2. Optical scattering properties

We have studied the angular distribution of scattered light for both series of KDP(Pr) and KDP(P) crystals in two regimes of excitation: (a) resonant regime at 532 nm and (b) nonresonant one at 633 nm. The measurements were carried out only in the forward hemisphere, i.e. in the angle range $0 \leqslant \theta \leqslant 90°$. The laser beams propagated along the optical axis ($\theta = 0$) for Z-cut single crystals. We performed the axial rotation of the crystalline plates and observed the same angular distribution of the scattered light (isotropic character of the effect).

The measured scattering indicatrices for the series of KDP(P) crystals are presented at Fig. 3. Squares corresponds to the angular distribution of the scattered radiation of the laser beams propagating in air at 532 nm (*a*) and 633 nm (*b*). The data are presented on the semilogarithmic scale in order to cover a huge dynamic range of the described process – about 6–7 orders of the signal magnitude reduction at large scattering angles. All the data are normalized on the total transmitted power P_0 in the forward hemisphere. It was estimated by the incident power of the laser sources and the total transmittance data presented at Table 1.

Due to the spatial averaging effect of the lens attached to the CCD array, all the curves look like very similar: a sharp bell-shaped part and wings. In order to understand the physical origin of each part, we present the data for the KDP(P) series on the double logarithmic scale (see Fig. 4). One can clearly see how the presence of the lens distorts the shape of the registered indicatrix. One can split each curve into three typical ranges, where the investigated dependences are distorted at different extents.

The first one ($\theta \leqslant 1°$) is a plateau. In this "blurred" interval, the lens collected almost the whole laser beam transmitted through the sample – the so-called ballistic photon registration geometry. Thus, the acquired data do not depend on the angular position of the lens. It is the range of the biggest distortions, because, according to the spatial averaging, no peculiarities in the indicatrix can be resolved at such small angles.

In the second interval $1° \leqslant \theta \leqslant 2°$, an abrupt decrease of the registered signal is observed, when the lens departs from the transmitted laser spot area. This corresponds to the direct light to shadow angular range scan with large experimental errors (up to 20%) due to the angular position uncertainty $\Delta\theta$ of the measuring unit.

In the third interval $\theta \geqslant 2°$, the lens collects only the light scattered by a sample. For a medium without spatially periodic structures, the angular distribution of the scattered light is smooth on the logarithmic scale. Thus, the spatial averaging of the collecting lens has no essential impact on the angular resolution of a registered signal. A slight reduction of the angular resolution is compensated by the essential enhancement of a registered signal level.

In the third interval (Fig. 4), we observed an almost linear decrease of the registered signal on the double logarithmic scale. This corresponds to the wing parts of the same dependences plotted on the semilogarithmic scale in Fig. 3. The slope -2.0 ± 0.3 ($2° \leqslant \theta \leqslant 45°$) is the same for the different series of samples and for the different readout wavelengths. This means that the scattered radiation power along the θ direction obeys the inverse quadric law $\Delta P(\theta) \sim \theta^{-2}$.

Due to negligible distortions of the angular distribution of scattering data in the mentioned intervale, the registered indicatrix is very similar to the real one. This enables us to estimate the scattering losses in the forward hemisphere p_{scat} for all samples under study. The method of calculation is based on the integration of the scattered light power $\Delta P(\theta)$ in the solid angle $\Delta\Omega$ over the part of the forward hemisphere that corresponds to the 3rd scattering area in Fig. 4,

$$p_{\text{scat}} = \frac{2\pi}{P_0} \int\limits_{\theta_{\min}}^{\pi/2} \frac{\Delta P(\theta)}{\Delta\Omega} \sin\theta d\theta, \tag{1}$$

where the lens incoming solid angle $\Delta\Omega = 4\pi \sin^2 \theta_{\text{lens}}/2 = 1.8 \times 10^{-3}$ sr, $\theta_{\min} \sim 1.8°$ exceeds the lens angular aperture $\theta_{\text{lens}} = \text{arctg}(d/2L) \sim 1.4°$ due to a finite size of the transmitted beam at the registration plane. The data were normalized on the total power P_0 transmitted into the forward hemisphere.

The results of estimations of the scattering losses p_{scat} via Eq. (1) are presented in Table 2. The pure P and Pr single crystals scatter about 1% of the light radiation for both laser wavelengths. The ten-percent increase of the losses in the Pr crystal in comparison with the P one can be attributed to a higher concentration of impurities in the former [1]. The incorporation of TiO_2 nanoparticles insignificantly reduces the optical quality of the crystals. Even for 10^{-3} TiO_2 wt.% concentration, the scattering losses do not exceed 3% that makes it possible to utilize the hybrid crystals for the different optical applications.

T a b l e 2. Scattering losses into the forward hemisphere for KDP:TiO_2 crystals series normalized on total power P_0 transmitted into the forward hemisphere, %

	Pure KDP	TiO_2 conc., wt.%		
		10^{-5}	10^{-4}	10^{-3}
P (633 nm)	1.0	1.7	1.8	–
Pr (633 nm)	1.1	2.6	2.6	2.6
P (532 nm)	1.0	1.7	2.5	–
Pr (532 nm)	1.1	1.7	1.3	2.8

In order to explain the obtained data on scattering losses, we should refer to the structural characterization of the hybrid media. The high-resolution X-ray diffraction analysis has shown that the incorporation of nanoparticles has no essential effect on the structural perfection of composite materials [1]. In the growth process, the KDP matrix can capture nanoparticles between the growth layer stacks, by effectively forming a 1D layered macroscopic structure ... KDP:TiO_2:KDP... with a spatial period of 20–30 μm. This gives possibility to incorporate TiO_2 nanocrystals, whose nonlinear optical response can be controlled by the resonant excitation of surface states [2].

Thus, the anatase nanocrystals are distributed on the planes of the boundaries of KDP growth layer stacks with a definite spatial period. The orientations of these planes relative to the optical axis are different for the P and Pr series. In the Z-cut plates, the optical axis is parallel to the planes of boundaries with TiO_2 nanoparticles for the Pr crystals, and it makes an angle of about 44° for the P one.

For the nonresonant readout case, the scattering losses at 633 nm in both series of KDP(P) and KDP(Pr) crystals are almost independent of the TiO_2 concentration. A reduction of the scattering losses by $\sim$ 30% in the P series can be explained by the tilt of the planes with TiO_2 nanoparticles toward the laser beam propagation (optical axis) direction, which leads to a decrease of the interaction length of light with nanoparticles.

In the case of the resonant excitation at 532 nm, the effect from TiO_2 nanoparticles is evident. It is clearly seen in Fig. 3 for the P series at the part with indicatrix wings. The scattering losses at 532 nm (a) are higher for the crystals with incorporated nanoparticles as compared with those for the pure one. But, in the case of the 633-nm irradiation (b), they are much alike. The noise level reference of the acquisition unit corresponds to the wings of the laser beam scattering indicatrix.

The monotone growth of the scattering losses with the concentration of nanoparticles for the P series is determined by the following. The preliminary research has shown that the KDP:TiO_2 single crystals manifest a self-focusing effect with the CW laser excitation at 532 nm due to the resonant excitation of anatase nanoparticles.

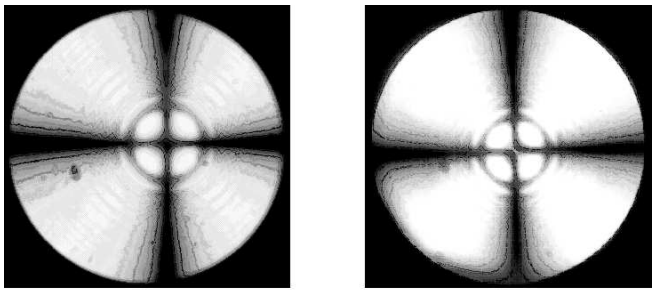

Fig. 5. Cone-shaped interference images for Z-cut plates of (a) pure KDP(P), (b) KDP:TiO_2 (P-4) single crystal plates

The effect leads to the optical contrast enhancement in a vicinity of the nanocrystal and to an increase of its scattering cross-section.

The same effect in conjunction with a specific alignment of nanoparticles toward the beam propagation direction produces a more complicate response to a variation of the concentration of nanoparticles in the Pr series. An increment of the refractive index at the boundaries of KDP growth layer stacks with TiO_2 nanoparticles leads to the waveguiding effect along the beam propagation direction inside KDP layers. The photoinduced waveguiding effect reduces the scattering of light: at least by 30% for Pr-5 and by a factor of two for Pr-4 (see Table 2) as compared with the nonresonant excitation case.

The Pr-4 sample possesses unique useful optical properties among the rest investigated KDP crystals with incorporated TiO_2 nanoparticles: enhanced transmittance in the UV-visible range and low scattering losses at the 532-nm resonant laser excitation.

3.1.3. Cone-shaped interference analysis

Pure KDP belongs to uniaxial negative crystals. The incorporation of TiO_2 nanoparticles produces additional stresses/strains in crystals. Due to this fact, the crystals acquire the anomalous biaxiality (AB) which can be measured for Z-cut plates within the cone-shaped interference analysis. The technique is the following: a sample is mounted between crossed polarizers, and it is illuminated with a cone-shaped beam.

The cone-shaped interference images for Z-cut plates of pure KDP(P) (a) and P-4 (b) samples are presented in Fig. 5. For isotropic media like pure KDP(P), two isogyres overlap along the optical axis and form the dark cross (a). The incorporation of nanoparticles induces the AB effect and a lateral optical anisotropy. The last one exhibits itself as the isogyre divergence (b). The extent of the AB effect is determined from the magnitude of isogyre divergence (the angle $2V$) in a cone-shaped interference pattern.

The distance between the isogyres is independent of the rotational orientation of a sample and depends on the $2V$ value of a material. When this $2V$ value is large (about 40–50°), two isogyres are rarely seen at a single image. However, for materials with a weak AB effect, the $2V$ value is small and can be measured directly from the image.

Values of $2V$ were measured for KDP(P) crystals over different lateral points of samples. The results are summarized in Table 3. They show that the strains in pure KDP single crystals are very small. The manifestation of the AB effect enhances with increase in the concentration of incorporated TiO_2 nanoparticles in the matrix. However, even for 10^{-4} TiO_2 wt.%, the value of $2V$ is less than $20'$, which indicates a good optical quality of the samples under study.

3.2. The mathematical model

As was shown above, the registered scattering indicatrices are distorted by the presence of the lens, especially in areas 1 and 2 in Fig. 4. Let θ_0 denote the current position of the lens center. Then the registered dependences $P(\theta_0)$ are quite precise at $\theta_0 > 2°$. But, at small angles, they need an additional processing. When the "wings" of indicatrices are compared on the logarithmic scale, the central part $|\theta_0| \leqslant 2°$ should be given on a linear scale for convenience.

There are two possible ways to obtain the real view of the indicatrix at $\theta_0 \leqslant 2°$. The first way is experimental (using an optical fiber spectrophotometer instead of a CCD with a lens), and the second one is a way of mathematical processing. The first way is rather complicated and requires a lot of time to execute experiments. So it is reasonable to develop a simulation procedure to solve this problem, and the current mathematical model is the first step on this way. The verification of the model was performed, by using a 532-nm continuous laser and the series of KDP(P) crystals.

T a b l e 3. Results of the cone-shaped interference analysis for KDP(P) series

TiO_2 conc., wt.%	Intrinsic strain anomalies (number of points)				$2V_{av.}$
	0–56′	5–10′	10–15′	15-20′	
0	60	40	–	–	6
10^{-5}	–	–	80	20	12
10^{-4}	–	–	40	60	17

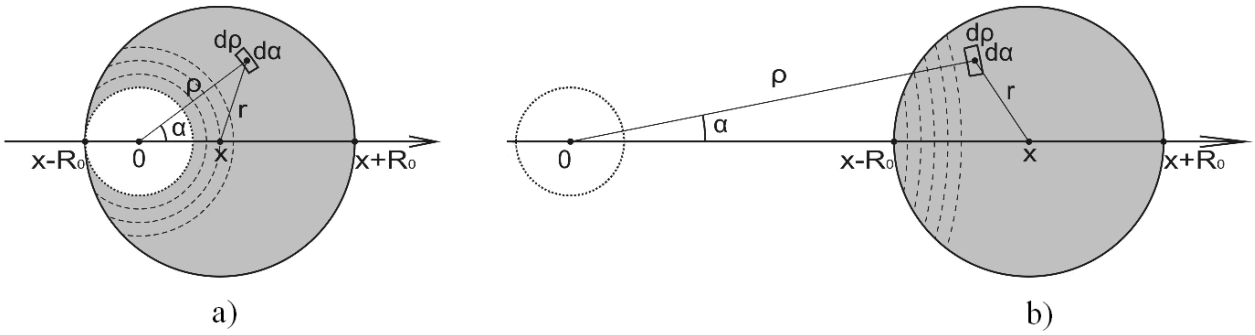

Fig. 6. Lines of equal radiation intensities on the lens: when the laser beam axis is in (*a*) and beyond (*b*) the lens aperture

For isotropic samples, the intensity distribution of scattered radiation is axially symmetric, so the lines with the same intensity are circumferences of radii $\rho = L\sin\theta$ (Fig. 6), where θ is the azimuth angle, and L is the distance between the sample and the lens (Fig. 1). As the registration unit moves along a circle, it is reasonable to use a spherical coordinate system. But, to process the data registered at the rotation angles $|\theta_0| \leqslant 2^\circ$ of a movable goniometer arm, a cylindric coordinate system can be used. The coordinate origin O is the point where the laser beam axis hits the center of a lens at $\theta_0 = 0$. Then, at $\theta_0 \neq 0$, the lens center coordinate $x = L\sin\theta_0 \approx L\theta_0$ (Fig. 6), α is the polar angle, and r is the distance from an arbitrary point on the lens aperture to the lens center. The laser beam axis in Fig. 6 is perpendicular to the plane of the figure.

For convenience, $u(x)$ in the mathematical part of the work means the registered scattered power $\Delta P(\theta_0)$, and $\nu(\rho)$ stands for the real scattered intensity $I_{\rm scat}(\theta)$. Then the infinitesimal amount of a registered radiation power at each point of the lens can be given by

$$\Delta u = \nu(\rho)G(x,\rho,\alpha)\Delta S, \tag{2}$$

where G is the propagation function at a specific point on the lens, and ΔS is an area element of the lens aperture (Fig. 6).

The integration of Eq. (2) over the lens aperture gives the registered radiation power at a certain position θ_0 of a CCD with a lens. If we assume that the propagation function depends only on the polar radius of a point on the lens $G = \hat{G}(r)$, we can write

$$u(x) = \int\limits_{\rho_1(x)}^{\rho_2(x)} \rho\nu(\rho) \int\limits_{\alpha_1(x,\rho)}^{\alpha_2(x,\rho)} G(x,\rho,\alpha)d\rho d\alpha, \quad x \in [-a,a]. \tag{3}$$

Here, $G(x,\rho,\alpha) = \hat{G}(r)$ according to

$$r^2 = \rho^2 + x^2 - 2\rho x\cos\alpha. \tag{4}$$

According to the geometry of the experiment ($L = 200$ mm, $a \leqslant 7$ mm), Eqs. (3)–(4) are written with an error less than 0.08 %.

The dependence $\hat{G}(r)$ can be directly measured if an ideally thin laser beam scans the lens along its diameter. In this case, at a point $r = R_0$ ($R_0 = d/2$ is the lens radius), the abrupt drop in a registered signal from a finite value to zero would be observed. But, by mathematical reasons, $\hat{G}(r)$ should be continuous at every point of $r \in [0, +\infty)$, and this abrupt drop should be eliminated.

As the laser beam diameter $\delta \approx 0.9$ mm is sufficiently less than the lens size, the experimental data for a freely propagating laser beam were taken as a propagation function. It can be approximated with a continuous function, and its form is similar to the real propagation function because $\delta \ll d$. The results of the experimental measurements are shown in Fig. 7. As a mathematical approximation, we use the function

$$\hat{G}(r) = \chi(R_1^2 - r^2)(A\exp((r/r_A)^2) -$$

$$-(r/r_B)^2 - C\exp(-\frac{(r/r_C)^2}{1-(r/r_H)^2})\chi(r_H^2 - r^2)), \tag{5}$$

where $R_1 = 5.509$ mm,

$$A = 2.223, \qquad r_A = 5.808 \text{ mm}, \ C = 1.277,$$
$$r_B = 2.357 \text{ mm}, \ r_C = 3.574 \text{ mm}, \ r_H = 4.711 \text{ mm},$$

and $\chi(s)$ is the Heaviside function equal to unity for $s \geqslant 0$ and equal to zero for $s < 0$.

In Eq. (5), we have $\hat{G}(r) \equiv 0$ for $r > R_1$. Here, $R_1 > R_0$, because the beam radius is non-zero. The relative approximation error is 3.6%, while the relative experimental error is $\approx 5\%$.

From the symmetry in Fig. 6, it is clear that, in Eq. (3), $\alpha_1(x,\rho) = -\alpha_2(x,\rho)$. Using Eq. (4), we can

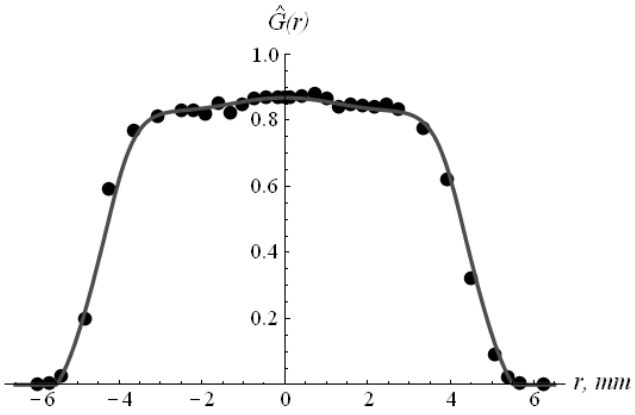

Fig. 7. Propagation function of the experimental setup (solid line) and experimental data for a freely propagated beam (dots)

write

$$\alpha_2(x,\rho) = \begin{cases} \arccos\left(\frac{\rho^2+x^2-R_1^2}{2\rho x}\right), & \rho + x > R_1, \\ \pi, & \rho + x \leqslant R_1. \end{cases} \quad (6)$$

Using Eq. (6) and the function $G(x,\rho,\alpha)$, one can found the inner integral in Eq. (3). As $G(x,\rho,\alpha)$ is a symmetric function, it can be written as

$$K(x,\rho) = \frac{1}{2}\int\limits_{\alpha_1(x,\rho)}^{\alpha_2(x,\rho)} G(x,\rho,\alpha)d\alpha = \int\limits_{0}^{\alpha_2(x,\rho)} G(x,\rho,\alpha)d\alpha. \quad (7)$$

Equation (7) enables us to write the integral relationship Eq. (3) in the form

$$u(x) = 2\int\limits_{\rho_1(x)}^{\rho_2(x)} \rho\nu(\rho)K(x,\rho)d\rho, \qquad x \in [-a,a]. \quad (8)$$

As for determining the integration limits $\rho_1(x)$ and $\rho_2(x)$, two positions of the lens with respect to the center of a laser beam are possible. In the first case, the center of the beam lies inside the circle of the radius R_1 (Fig. 6,*a*, $x \leqslant R_1$). In the second case, the center of the beam is outside the circle (Fig. 6,*b*, $x > R_1$). At first, we discuss both of the cases apart.

1) $x \leqslant R_1$.

According to Eq. (6), in this case, the lines of equal radiation intensities inside the circle with R_1 may be of two types:

a) Circumferences of radii $0 \leqslant \rho \leqslant (R_1 - x)$. Then $\alpha_2(x,\rho) = \pi$ and

$$K_0(x,\rho) = \int\limits_0^{\pi} G(x,\rho,\alpha)d\alpha,$$

$$u(x) = 2\int\limits_0^{R_1-x} \rho\nu(\rho)K_0(x,\rho)d\rho. \quad (9)$$

b) Arcs of the circumferences $(R_1 - x) < \rho < (R_1 + x)$. Then $\alpha_2(x,\rho) < \pi$ according to Eq. (6) and

$$K_1(x,\rho) = \int\limits_0^{\alpha_2(x,\rho)} G(x,\rho,\alpha)d\alpha,$$

$$u(x) = 2\int\limits_{R_1-x}^{R_1+x} \rho\nu(\rho)K_1(x,\rho)d\rho. \quad (10)$$

The functions $K_0(x,\rho)$ and $K_1(x,\rho)$ are presented in Fig. 8. They can be united into a 2D continuous function $K(x,\rho)$.

2) $x > R_1$.

In this case, the lines of equal radiation intensities are also arcs of the circumferences with radii $(x - R_1) < \rho < (x + R_1)$. Here, $u(x)$ can be given identically to Eq. (10), but with different integration limits. The total integration relation Eq. (8) can be written using Eqs. (9)–(10) and Eq. (5) as follows:

$$u(x) = 2\int\limits_0^{2R_1} \rho\nu(\rho)K(x,\rho)d\rho, \qquad x \in [-a,a], \quad (11)$$

where $K(x,\rho)$ is the union of the functions $K_0(x,\rho)$ and $K_1(x,\rho)$ (Fig. 8).

There are two ways to interpret Eq. (11). When the real intensity distribution of the scattered light $\nu(\rho)$ is known, Eq. (11) becomes the integration formula one can use to mathematically obtain the resulting data of the experiment with certain parameters of the laser setup. In this case, the direct problem is solved, and no computational difficulties arise.

Another situation appears at solving the inverse problem. Here, $u(x)$ is known, and the task is to reconstruct the real intensity distribution $\nu(\rho)$ of the radiation scattered by the sample. Then Eq. (11) serves as the Fredholm first-kind integral equation, and its solution is a solution of an incorrect problem. In this case, special regularization methods are required [6, 7].

At the stage of verification of the consistency of the mathematical model of the experimental laser setup for the optical diagnostics of low-dispersion samples, it is

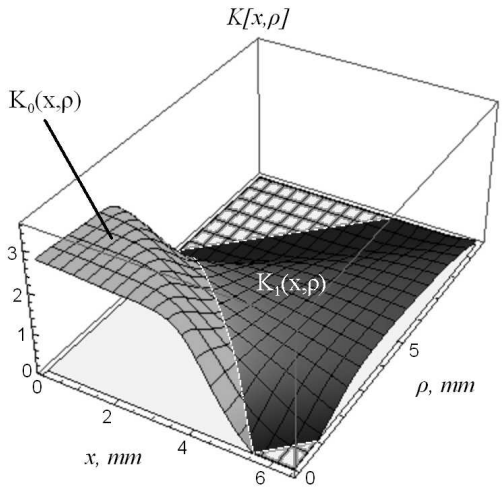

Fig. 8. Form of the integrand function $K(x, \rho)$

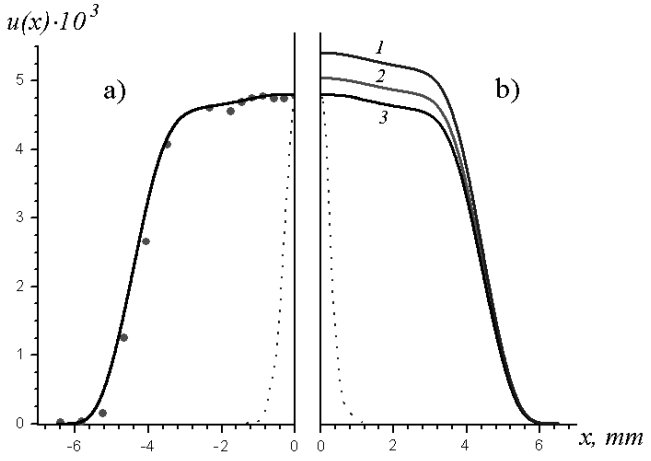

Fig. 9. Comparison of the experimental data at 532 nm and the simulation results. (*a*) Dots – experimental data for P-4 sample, solid line – simulation, dashed line — precise measurements (normalized for convenience). (*b*) Simulation results: *1* – freely propagated laser beam, *2* – KDP(P) pure, *3* – P-4 sample

suitable to have the experimental data for $\nu(\rho)$ and $u(x)$. For this purpose, we studied

a) Freely propagated 532-nm laser beam;

b) Laser beam passes through a pure KDP(P) crystal;

c) Laser beam passes through a KDP crystal doped with TiO_2 nanoparticles (sample P-4).

To experimentally obtain the data on the real intensity distribution $\nu(\rho)$, we used the experimental setup with an optical-fiber (diameter $d = 410$ μm) spectrophotometer instead of a CCD with a lens. Results of the experiment reveal that, in all three investigated cases, the propagating laser beam has the Gaussian intensity distribution

$$\nu(\rho) = \exp(-(\rho/\rho_0)^2). \tag{12}$$

A beam size reduction in the registration plane after the transmission of samples at 532 nm was shown ($\rho_0 = 0.447$ mm in the case of free propagation of the beam). In case of KDP with TiO_2 (0.421 mm), it is less than that for pure KDP (0.432 mm). This can be explained by the photoinduced self-focusing effect in these samples at the 532-nm CW laser excitation, which will be published elsewhere in detail. This result proves that knowing the real scattering indicatrix can be essential for the optical characterization of a sample.

In Fig. 9,*a*, the experimental data (dots) and the calculated $u(x)$ dependence (solid line) for P-4 sample are presented. We also show the precise scattering data for P-4 sample (dashed line, normalized to $\sim 5 \times 10^{-3}$ for convenience). Figure 9,*b* shows the difference between the calculated indicatrices for a freely propagated laser beam, pure KDP(P), and P-4 sample. The result presented is in good agreement with spectral data (Table 1). The dependences $u(x)$ for all the samples are obtained, by using Eq. (11) and functions (12), the approximation error being less than 5%.

Based on the results of the work, it can be stated that the mathematical model of the experimental laser setup for the optical diagnostics of low-dispersion samples is consistent, and it can serve as a base for developing a way to solve the inverse problem, i.e. to get the real scattering data $I_{\text{scat}}(\theta)$ out of the registered $\Delta P(\theta_0)$ using mathematical calculations.

4. Summary

In this work, the optical characterization of series of KDP crystals doped with TiO_2 nanoparticles (anatase modification) in various concentrations was performed. The characterization includes measurements of scattering indicatrices and optical transmission spectra and the cone-shaped interference method.

The investigations show that the incorporation of TiO_2 nanoparticles slightly changes the optical quality of KDP crystals. All of the characterization results contribute to a good optical quality of the investigated samples: transmittances in the visible range $\sim$ 90%, scattering losses $< 3\%$, and the anomalous biaxiality values $2V < 20'$.

A mathematical model of the experimental setup was developed in order to enhance the angular resolution in

the scattering indicatrices at angles $\theta \leqslant 2^\circ$, where the registered data are blurred due to the presence of a lens in the measuring circuit. The model was verified in the direct way and showed itself to be consistent with an error less than 5%.

The work was supported by STCU-NASU grant No. 4956.

1. I. Pritula, V. Gayvoronsky, M. Kopylovsky *et al.*, Func. Mat. **15**, 420 (2008).
2. V. Gayvoronsky, A. Galas, E. Shepelyavyy *et al.*, Appl. Phys. B **80**, 97 (2005).
3. A.O. Borshch, M.S. Brodyn, V.Ya. Gayvoronsky *et al.*, Ukr. J. Phys. **49**, 196 (2004).
4. V.Ya. Gayvoronsky, M.A. Kopylovsky, E.A. Vishnyakov *et al.*, Func. Mat. **16**, 136 (2009).
5. I.N. Ogorodnikov, V.Yu. Yakovlev, B.V. Shul'gin and M.K. Satybaldieva, Phys. Solid State **44**, 880 (2002).
6. A.N. Tikhonov and V.Ya. Arsenin, *Methods of Solution of Ill-Posed Problems* (Nauka, Moscow, 1979) [in Russian].
7. V.N. Starkov, *Constructive Methods of Computational Physics in Interpretation Problems* (Naukova Dumka, Kyiv, 2002) [in Russian].

Received 01.06.10

ХАРАКТЕРИЗАЦІЯ ОПТИЧНОЇ ЯКОСТІ КРИСТАЛІВ KDP З ІНКОРПОРОВАНИМИ НАНОЧАСТКАМИ TiO_2 ТА МОДЕЛЮВАННЯ ЛАЗЕРНОГО ЕКСПЕРИМЕНТУ З РОЗСІЯННЯ

В.Я. Гайворонський, В.М. Старков, М.А. Копиловський, М.С. Бродин, Є.О. Вишняков, О.Ю. Боярчук, І.М. Притула

Р е з ю м е

Досліджено індикатриси розсіювання в чистих кристалах KDP та в KDP з інкорпорованими наночастками діоксиду титану. Показано, що оптична якість кристалів знижується несуттєво для досліджуваних концентрацій наночасток. Розроблено та обговорено математичну модель експериментальної установки для вимірювання розсіяння світла у слаборозсіюючих середовищах. Апаратна функція експериментальної установки подана в аналітичній формі. Відповідність моделі перевірено з використанням експериментальних даних з розсіяння.